PNAS RESEARCH ARTICLE | BIOPHYSICS AND COMPUTATIONAL BIOLOGY

Deciphering molecular mechanisms stabilizing the reovirus-binding complex

Rita dos Santos Natividade[a,1], Melanie Koehler[a,b,1], Priscila S. F. C. Gomes[c], Joshua D. Simpson[a], Sydni Caet Smith[d], Diego E. B. Gomes[c], Juliette de Lhoneux[a], Jinsung Yang[a], Ankita Ray[a], Terence S. Dermody[e,f,g], Rafael C. Bernardi[c,2], Kristen M. Ogden[d,h,2], and David Alsteens[a,i,2]

Edited by Peter Palese, Icahn School of Medicine at Mount Sinai, New York, NY; received December 7, 2022; accepted April 6, 2023

Mammalian orthoreoviruses (reoviruses) serve as potential triggers of celiac disease and have oncolytic properties, making these viruses potential cancer therapeutics. Primary attachment of reovirus to host cells is mainly mediated by the trimeric viral protein, σ1, which engages cell-surface glycans, followed by high-affinity binding to junctional adhesion molecule-A (JAM-A). This multistep process is thought to be accompanied by major conformational changes in σ1, but direct evidence is lacking. By combining biophysical, molecular, and simulation approaches, we define how viral capsid protein mechanics influence virus-binding capacity and infectivity. Single-virus force spectroscopy experiments corroborated by in silico simulations show that GM2 increases the affinity of σ1 for JAM-A by providing a more stable contact interface. We demonstrate that conformational changes in σ1 that lead to an extended rigid conformation also significantly increase avidity for JAM-A. Although its associated lower flexibility impairs multivalent cell attachment, our findings suggest that diminished σ1 flexibility enhances infectivity, indicating that fine-tuning of σ1 conformational changes is required to successfully initiate infection. Understanding properties underlying the nanomechanics of viral attachment proteins offers perspectives in the development of antiviral drugs and improved oncolytic vectors.

biophysics | virus | atomic force microscopy | molecular dynamics | glycan

Significance

The initial attachment of viruses to cell-surface receptors serves as a primary determinant of the outcome of infection. However, the dynamics and cooperativity between viruses and multiple cell-surface receptors are still poorly understood. Focusing on reovirus, an oncolytic human virus, we discovered how the virus uses two different steps to initiate a successful infection. First, reovirus binds cell-surface sialic acid, which serves as a molecular bridge between the virus and the cell surface. Second, reovirus adopts more extended protein conformers, yielding a more stable molecular complex that favors virus entry. The in vitro and in silico data presented provide biophysical insights into the dynamics and outcomes of viral attachment to cellular receptors.

Mammalian orthoreoviruses (reoviruses) are nonenveloped, icosahedral viruses (~85 nm) that contain a segmented, double-stranded (ds) RNA genome (1). While not commonly associated with human disease, reovirus infection appears to trigger the development of celiac disease by disrupting the induction of immunological tolerance to orally ingested gluten (2). In addition, reovirus shows oncolytic activity across a range of tumor types (3). Clinical trials have demonstrated that reovirus-based therapeutics are safe and show efficacy when administered in combination with other anticancer treatments (4, 5). However, a better understanding of reovirus entry mechanisms would help improve their functionality as therapeutic agents.

To productively infect host cells, a virus must locate and attach to cell-entry receptors that allow uptake and penetration of the cell membrane. For most viruses, this is not a simple one-step process, but rather a succession of tightly regulated steps involving binding partners on the surface of the virus and host cell (6–8). Reovirus binding to cells is predominantly mediated by outer-capsid protein σ1. The σ1 protein is a 150 kDa homotrimeric molecule that assembles into a long fiber that protrudes from the surface of the viral particle (VP) at the icosahedral fivefold vertices and is partitioned into three domains (tail, body, and head) (Fig. 1*A*) (9–11). The N-terminal tail is predicted to form an α-helical coiled-coil, the body domain consists of β-spiral repeats, and the C-terminal head folds into a compact domain composed of eight antiparallel β-strands. For reovirus strain type 1 Lang (T1L), the glycan binding site resides in the σ1 head domain (Fig. 1*A*, dark blue) and displays preferential affinity for branched glycan GM2 (12). The σ1 head domain also binds to junctional adhesion molecule-A (JAM-A), which serves as an entry receptor for all known reovirus serotypes (Fig. 1*A*, violet) (13–16). After attachment to cell-surface glycans, reovirus virions undergo lateral particle diffusion to bind with higher affinity to this proteinaceous receptor. We discovered that binding of reovirus strain type 3 Dearing (T3D) virions to glycans triggers a conformational change in σ1 to a more extended form, increasing its overall avidity for JAM-A (14). Such a conformational change also has been demonstrated by cryo-electron microscopy for T1L infectious subvirion particles (ISVPs), which are reovirus disassembly intermediates that can be produced in vitro by proteolytic digestion (17, 18). However, this change in avidity has not been characterized from a mechanistic and functional point of view.

In this study, we used an innovative approach to characterize, at a single-molecule level, the influence of conformational flexibility in the binding properties of σ1 in a cellular context. Combining force distance–based atomic force microscopy (FD-based AFM),

Author contributions: R.d.S.N., M.K., P.S.F.C.G., J.D.S., T.S.D., R.C.B., K.M.O., and D.A. designed research; R.d.S.N., M.K., J.D.S., S.C.S., D.E.B.G., J.d.L., J.Y., A.R., and K.M.O. performed research; R.d.S.N., M.K., P.S.F.C.G., J.D.S., S.C.S., D.E.B.G., J.d.L., J.Y., A.R., R.C.B., K.M.O., and D.A. analyzed data; and R.d.S.N., M.K., P.S.F.C.G., J.D.S., S.C.S., T.SD., R.C.B., K.M.O., and D.A. wrote the paper.

The authors declare no competing interest.

This article is a PNAS Direct Submission.

[1]R.d.S.N. and M.K. contributed equally to this work.

[2]To whom correspondence may be addressed. Email: rcbernardi@auburn.edu, kristen.ogden@vumc.org, or david.alsteens@uclouvain.be.

This article contains supporting information online at https://www.pnas.org/lookup/suppl/doi:10.1073/pnas.2220741120/-/DCSupplemental.

Published May 15, 2023.

single-particle tracking (SPT), and steered molecular dynamics (SMD), we determined how T1L VPs or ISVPs or T1L VPs containing σ1 cross-linked at various positions in the σ1 trimer bind to JAM-A and defined how conformational flexibility influences virus binding, diffusion, and infectivity. AFM and SMD results revealed that although GM2 appears not to affect σ1–JAM-A dynamics and force stability, GM2 engagement increases the binding affinity of σ1 to JAM-A by stabilizing residue contacts at the interface of the complex. While GM2 does not substantially alter reovirus binding to JAM-A in vitro, a higher affinity is observed when the σ1 head domains are cross-linked together, both for purified receptor and intact cells. However, although we observed an increase in affinity, this cross-linking also is accompanied by an inhibition of multivalent interactions, as negative cooperativity occurs for multiple bonds in the cellular context.

Overall, our results support the emerging idea of a cooperative role of glycans in stabilizing the complex with its entry receptor and that conformational changes of viral surface proteins to an extended structure promote higher viral receptor–binding kinetics. However, some flexibility of the σ1 protein is also required to establish multiple binding contacts, which directly affects the capacity of the virus to bind cell surfaces and diffuse, as shown by cross-linking the σ1 head domain. In the development of oncolytic vectors, the controlled cross-linking of viral capsid proteins involved in binding to cell-entry receptors could open avenues to improve specific cell targeting.

Results and Discussion

Probing Reovirus T1L Binding to Purified JAM-A. To evaluate the binding of reovirus strain T1L to JAM-A, we used FD-based AFM and probed the interactions at the single VP level with immobilized purified JAM-A (Fig. 1 *A*–*C*). Virions were immobilized on the tip apex using a polyethylene glycol $(PEG)_{24}$ linker (see *SI Appendix*, Fig. S1*A* for grafting validation) and cyclically approached and retracted from JAM-A (Fig. 1*B*) (see *SI Appendix*, Fig. S1*B* for validation of the JAM-A surface). Specific adhesion events were sorted based on the rupture distance of the rupture event, i.e., at least 5 nm corresponding to the PEG-linker extension, that follows a worm-like chain stretching behavior (19, 20). First, we analyzed the binding frequencies (BF) of wild-type (WT) T1L VPs to JAM-A and obtained a BF of 11.1 ± 5.0% (mean ± SD, N ≥ 4), which is comparable to the frequencies previously observed for reovirus strain T3D (14). To validate the specificity of the interaction, we injected a JAM-A antibody over the binding surface, which led to a ≈ sixfold reduction in the BF (*SI Appendix*, Fig. S2).

As a conformational change of σ1 was observed for T3D after injection of free sialyloside (14) and for T1L ISVPs by cryo-electron microscopy, we evaluated the BF of T1L VPs and ISVPs following glycan engagement. BF analysis did not reveal significant changes relative to T1L VPs. GM2 injection led to a frequency of 8.9 ± 6.9% for T1L VPs, while T1L ISVPs bound with a frequency of 12.3 ± 3.1% and 12.28 ± 4.4% following addition of GM2 (Fig. 1*D*). These results were surprising in view of the previous findings regarding reovirus T3D (14), and we conducted a more detailed analysis of the kinetic parameters that characterize the binding energy landscape.

Dynamic force spectroscopy (DFS) experiments were conducted by varying the retraction speed to explore a wide range of loading rate (LR, applied force over time) followed by extracting the kinetic parameters describing the free-energy landscape of the interaction between T1L VPs or ISVPs and JAM-A (Fig. 1 *E*–*H*). Overall, the probed complexes withstood forces in the range of 25 to 500 pN across the full range of applied LRs. After extraction of both rupture force and LR for all specific unbinding events recorded for T1L VPs or ISVPs, with or without injection of GM2, the data points were displayed in DFS plots (Fig. 1 *E*–*H*). Furthermore, through previously established force histogram analysis (*SI Appendix*, Figs. S3 and S4), single rupture events were fitted with the Bell–Evans (BE) model (21, 22), allowing extraction of the unbinding rate (k_{off}) and the distance to transition state (x_u), both extrapolated to zero pulling force (F_0).

From the BE fit, we determined k_{off} and x_u values for each of the probed interactions (Fig. 1 *E*–*H*). For T1L VPs, T1L VPs+GM2, and T1L ISVPs+GM2, x_u values were similar. However, we noticed a slight reduction in x_u for ISVPs that we think is attributable to the extended conformation of trimeric σ1 observed by cryo-EM (17). T1L VPs and ISVPs display a similar k_{off}, while injection of GM2 appears to produce a slight decrease in k_{off} for both VP forms. We also assessed the association rate (k_{on}) by monitoring the effect of contact time on the BF (Fig. 1 *E*–*H*, *Inset*). By fitting the data with a monoexponential growth model (*Methods*) assuming that the receptor–bond complex can be approximated by pseudo-first-order kinetics (23), we obtained the various k_{on} values (Fig. 1 *E*–*H*). In these experiments, the addition of GM2 appears to only slightly influence JAM-A binding, with a slightly greater increase in k_{on} after the addition of GM2 to T1L VPs. These different behaviors are reflected in dissociation constants (K_D), which are in the same high-affinity range.

Collectively, these results suggest that the affinity of T1L for JAM-A is slightly enhanced by sialic acid engagement, for both VPs and ISVPs, which is in good agreement with virus-binding assays conducted using CHO JAM-A cells (*SI Appendix*, Fig. S5). However, this observation is in contrast to what was observed for strain T3D, for which JAM-A avidity was more dramatically enhanced in the presence of its glycan ligand, and suggests that the σ1 conformational change may not be as marked for T1L or beneficial to JAM-A binding.

Influence of GM2 on the T1L σ1–JAM-A Complex Dynamics. The twofold decrease in K_D observed while probing JAM-A binding after addition of GM2 suggests that glycans positively influence the stability of the σ1–JAM-A complex. To further confirm our initial observation, a model of the T1L σ1 protein trimer complexed with JAM-A in the presence and absence of the GM2 glycan was built using comparative modeling in a strategy previously developed (24). Structures of the T1L σ1 protein trimer in complex with JAM-A (PDB ID 4ODB) and T1L σ1 protein trimer coupled with GM2 (PDB ID 4GU3) were employed. An in silico single-molecule force spectroscopy approach (25) was then applied to investigate the effects of GM2 on the mechanostability of the complex. In this approach, SMD simulations were conducted using NAMD 3 (25) in a wide-sampling paradigm. During the pulling simulations, the N-terminal residues of each σ1 monomer were anchored, while one of the JAM-A proteins was pulled at constant velocity by its C-terminal residue (Fig. 2*A*). The simulations resulted in force vs. extension curves with similar peak force, but irregular behavior, showing clear rupture events at some intervals and multistep events at others (Fig. 2 *B* and *C*). For both systems, the existence of multiple shielded events was observed, indicating that the rupture might occur in multiple small steps. Due to the much higher resolution of the simulations, such multistep events cannot be investigated in vitro.

Building on the force versus extension curves, the BE model (22, 26, 27) for the probability distribution of a rupture event showed very similar behavior for both systems (Fig. 2*D*). The behavior is in line with the experimental DFS results in which injection of GM2 appeared not to affect the force

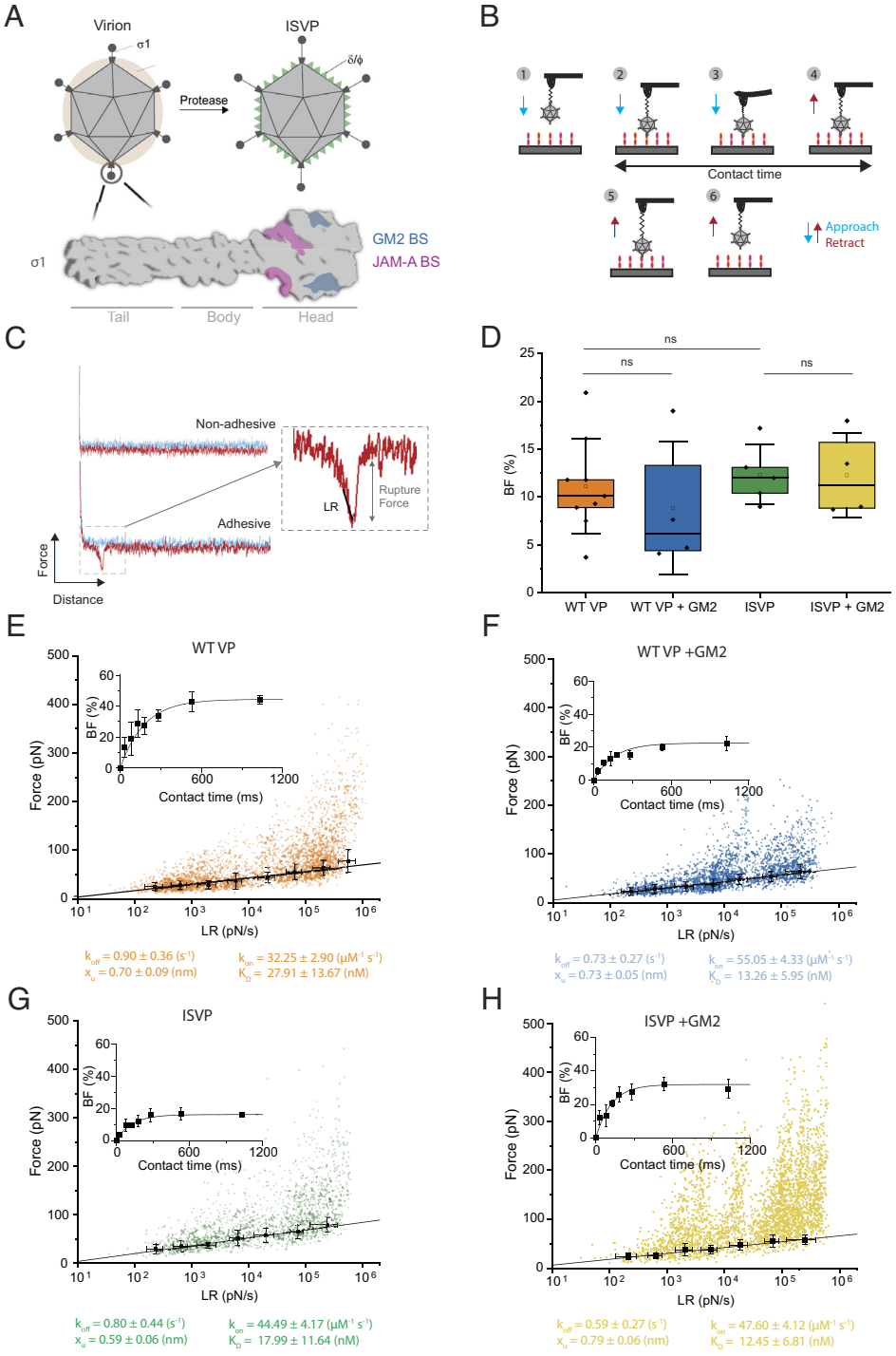

Fig. 1. Probing T1L binding to JAM-A on model surfaces. (*A*) Schematic representation of a T1L virion, with the σ1 protein mediating the binding to both GM2 and JAM-A, respectively, highlighted in dark blue and violet. Following proteolytic cleavage, the virion outer capsid is partially removed, generating the ISVP, which involves the release of σ3 subunits and cleavage of μ1 to the δ and φ fragments. In this form, σ1 adopts a more extended conformation. The σ1 trimer consists of three domains: tail, body, and head. (*B*) Schematic of probing a JAM-A-coated surface with an AFM tip functionalized with reovirus. First, the tip approaches the JAM-A surface (#1) until contact (#2). The tip continues to approach until a certain force threshold is reached (#3) and is then retracted (#4). In the case of a specific adhesion event, an elongation of the PEG linker is observed (#5) until the bond is ruptured, and the tip moves away from the surface (#6). (*C*) Representative FD curves recorded using the model surfaces showing nonspecific and specific adhesion events. Rupture forces are collected from the peak of an unbinding event. Loading rate (LR) corresponds to the slope of the curve just before rupture of the bond. (*D*) Box plot of the binding frequency (BF) between virions and the JAM-A-coated surface, calculated for WT T1L VPs, WT VPs after addition of GM2 (1 mM), T1L ISVPs, and T1L ISVPs after addition of GM2 (1 mM). One data point represents the BF obtained for one map of 1,024 FD curves. The horizontal line within the box indicates the median, boundaries of the box indicate the 25th and 75th percentiles, and the whiskers indicate the SD. Statistical significance was determined by two-sample *t* test. *P* values for the comparison between WT VPs and WT VPs + GM2 or ISVPs are 0.51 and 0.063, respectively. *P* value for the comparison between ISVPs and ISVPs + GM2 is 0.94. *P* values are represented by ns, $P > 0.05$. (*E*–*H*) DFS plots showing the distribution of the rupture forces as a function of their LR measured between JAM-A and (*E*) T1L VPs (N = 3,468 data points), (*F*) after injection of GM2 (N = 2,514 data points), (*G*) T1L ISVPs (N = 3,326 data points), and (*H*) ISVPs after injection of GM2 (N = 3,099). The solid line represents the fit of the data with the BE fit (for simple ligand–receptor bond), which provides average k_{off} and x_u values. The error bars indicate the SD of the mean. Binding frequency is plotted (as *Inset*) as a function of contact time. Data points represent mean BF calculated for each contact time and were fitted using a least-squares fit of a monoexponential decay, providing average values for the k_{on}, and the K_D is calculated using k_{off}/k_{on}. The error bars indicate SD. All data are representative of at least n = 3 independent experiments.

resilience of the complex over the applied LRs (Fig. 1 *E* and *F*). However, the DFS results also showed that GM2 injection slightly influences reovirus binding to JAM-A, which is reflected by the K_D values. To investigate the potential influence of GM2, we calculated the potential of mean force (PMF) on the σ1–JAM-A dissociation paths in the presence and absence of GM2 obtained from the SMD simulations. The PMF gives the free-energy profile along the reaction coordinate, capturing the energetics of the studied process (28). The PMF profile shows that the dissociation-free energy barrier in the presence of GM2 is approximately 25% higher than that in the absence of GM2 (Fig. 2*E*), revealing that GM2 influences the unbinding mechanism by stabilizing the σ1–JAM-A complex.

To better understand why the unbinding free energy barrier is larger in the presence of GM2, we examined the interface contact surface area between σ1–JAM-A interface residues, averaged over the SMD trajectories (Fig. 2*F*). This analysis suggested that the contact surface area after the first rupture event is higher in the presence of GM2 and that the glycan has a role in maintaining the complex stability for a longer period. Likewise, after the main rupture event, the average force shows a higher decrease in the absence of GM2 (Fig. 2*F*). These data corroborate the PMF profiles and the K_D values from the DFS experiments. From an energetic point of view, the work needed to rupture the complex becomes larger in the presence of GM2, as the force is applied for a longer time in the unbinding coordinate.

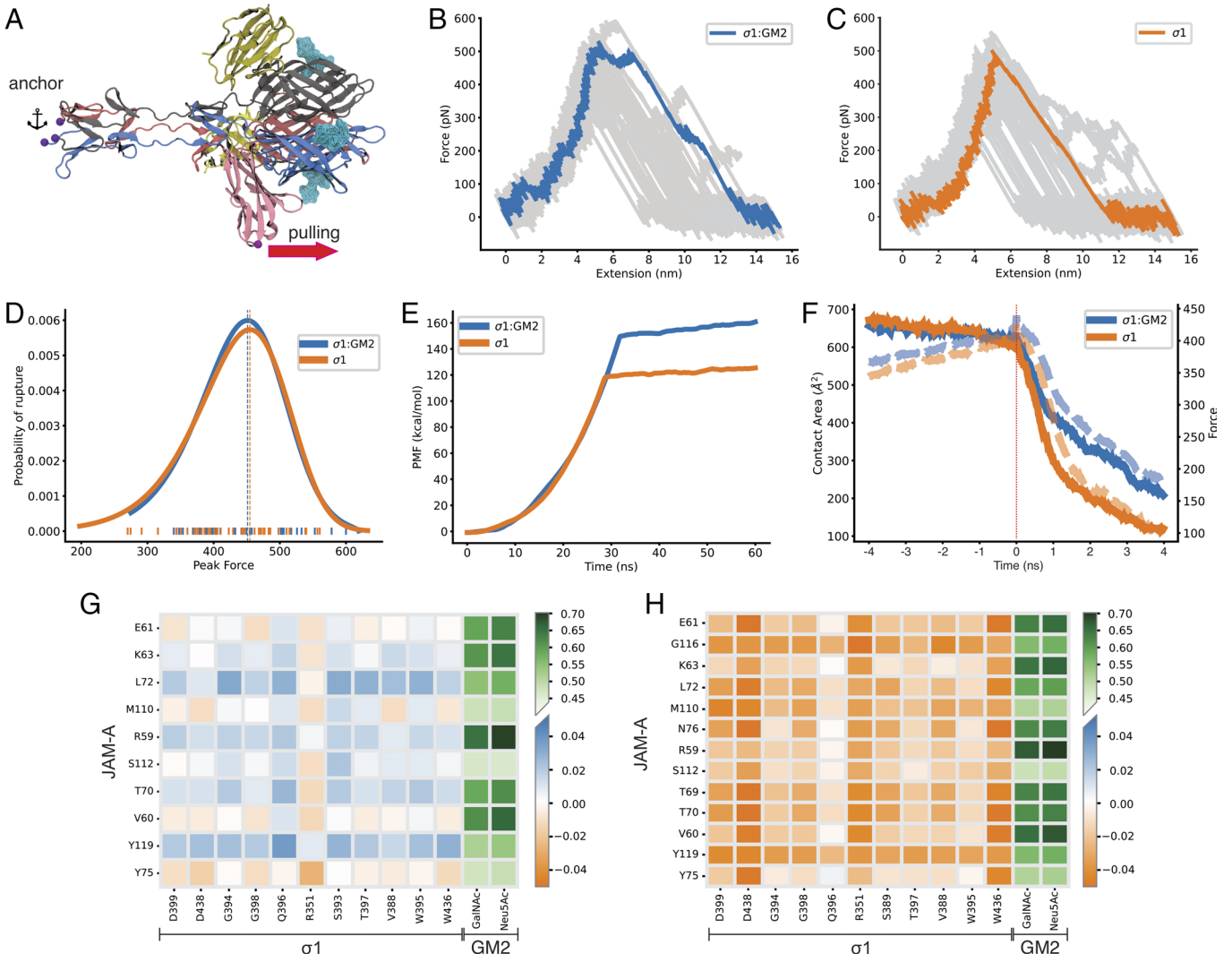

Fig. 2. Influence of GM2 on σ1–JAM-A dynamics. For simplicity, the models of JAM-A complexed with σ1 in the presence and absence of GM2 are labeled as σ1:GM2 and σ1. (*A*) Cartoon representation of the tridimensional structure model for the σ1 trimeric protein complexed with three copies of JAM-A and GM2. σ1 monomers are colored in blue, gray, and red; JAM-A-pulled molecule is colored in pink, while the other two molecules are colored in tan; GM2 molecules are represented as surface and colored in cyan. SMD anchor and pulling points are represented as spheres and colored in purple and magenta, respectively. The selected JAM-A molecule was pulled at a constant speed of 2.5×10^{-04} nm ps^{-1} with a 0.144 kcal mol^{-1}Å^2 spring constant. (*B* and *C*) Force versus extension curves for all replicas. Exemplary traces are highlighted in blue and orange. (*D*) BE model for the first rupture peak. (*E*) Potential of mean force (PMF) versus simulation time. (*F*) Contact area surface (full lines) and average rupture forces (dashed lines) calculated over the SMD trajectories, 4 ns before and after the main rupture event. (*G* and *H*) Difference in the mean correlation for the residue pairs in the σ1–JAM-A interface residues (orange to blue) and the glycan–JAM-A interface residues (light to dark green), before (*G*) and after (*H*) the main rupture event.

To shed light on how GM2 influences the interface, we investigated the σ1–JAM-A interface residues in more detail using the generalized correlation–based dynamical network analysis method (29). This analysis measures the correlation of the molecular motions between residues. The higher the correlation, the more relevant is their interaction for the stability of the protein complex (30). The difference in the mean correlation values between the interface residues, before and after the first rupture event (Fig. 2 *G* and *H*), shows no significant difference between the systems (±0.04). However, the GM2 moieties with α-linked 5-N-acetyl neuraminic acid (Neu5Ac) and N-acetylgalactosamine (GalNAc) display high correlation values with most of the JAM-A interface residues (0.40 to 0.70), even after the main rupture event (Fig. 2*H*). These results indicate that the presence of GM2 increases the stability of the σ1–JAM-A interface.

Influence of σ1 Cross-Linking on σ1–JAM-A Complex Stability. To precisely control the conformational change associated with the extension of σ1, which has occurred in ISVPs, and to evaluate the influence of this conformational change on the affinity of σ1 binding to JAM-A, we analyzed the behavior of T1L variant viruses harboring cysteine mutations in σ1. These mutations cross-link σ1 by establishing disulfide bonds between structurally adjacent sites within the tail, body, or head domains (31). Specifically, we tested T1L viruses containing engineered cysteine residues that cross-link the σ1 tail domain (Tail; N38C), body domain (Body; G287C, V299C), head domain (Head; M332C, S403C), and a fourth variant with cross-linking in the head domain and mutations that abrogate sialic acid binding (HeadΔSA; M332C, S403C, S370P, Q371E) (Fig. 3*A*). While FD-based AFM experiments confirm that Head and HeadΔSA mutants interact with JAM-A with higher BF, as previously observed (31), this was not observed for the Tail and Body mutants (Fig. 3*B*). We validated the specificity of the interactions using JAM-A antibodies in a blocking assay (*SI Appendix*, Fig. S6).

To understand the basis of the different BFs observed, we extracted the kinetic parameters using the methodology described above. Specific binding events were displayed in DFS plots (Fig. 3 *C*–*F*),

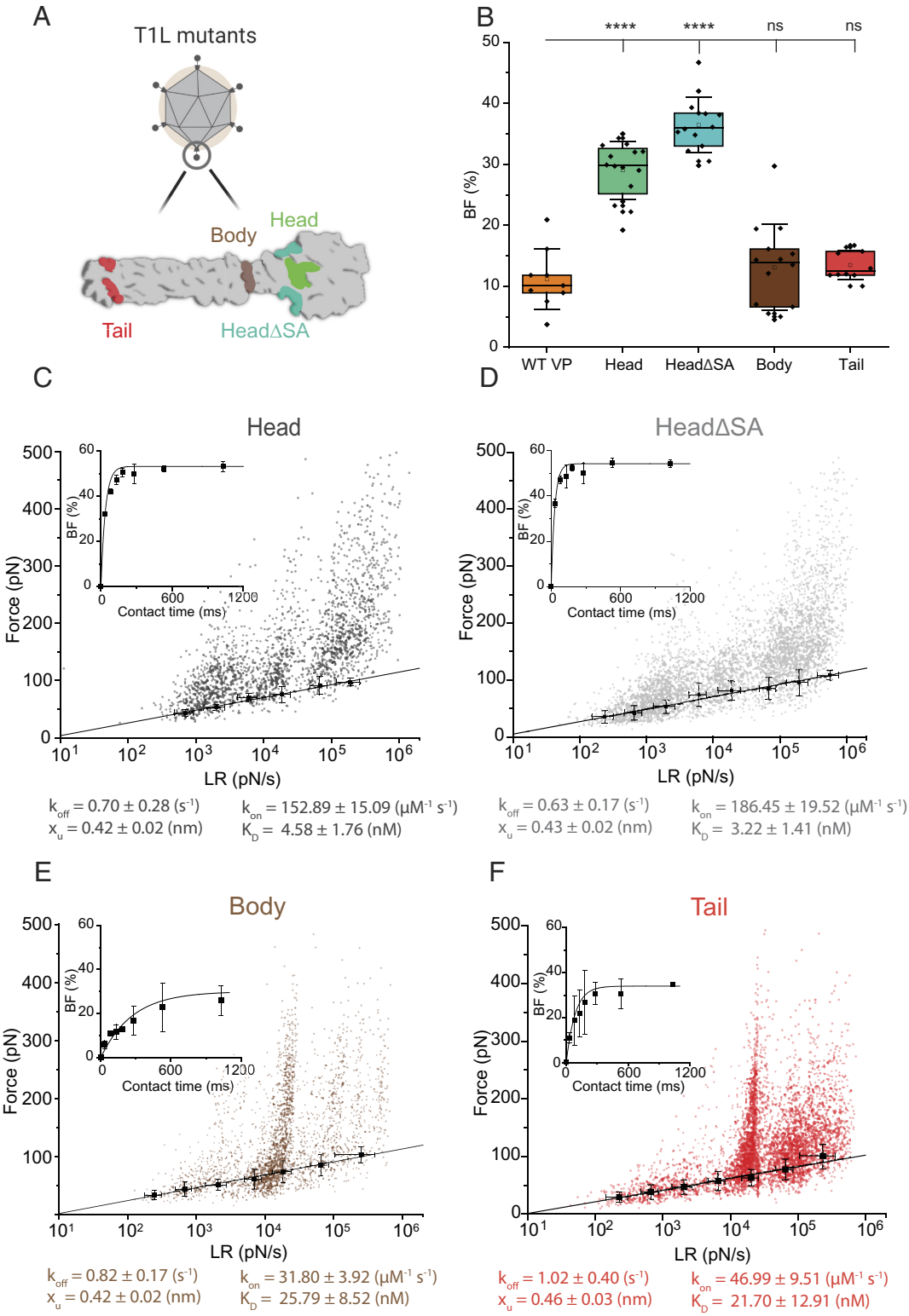

Fig. 3. Binding of engineered reovirus mutants to purified JAM-A. (*A*) Schematic representation of a T1L virion and space-filling model of σ1 showing locations of engineered cysteine mutations in the tail, body, and head domains. These mutations result in the formation of disulfide bridges between adjacent monomers within the σ1 trimer, leading to the cross-linking of different regions. (*B*) Box plot of the BF between VPs and JAM-A calculated for WT T1L, Head, HeadΔSA, Body, and Tail. The horizontal line within the box indicates the median, boundaries of the box indicate the 25th and 75th percentiles, and the whiskers indicate the SD. Statistical significance was determined by two-sample *t* test. *P* values for the comparison between WT T1L and Head, HeadΔSA, Body, or Tail are 6.29×10^{-9}, 3.07×10^{-11}, 0.48, and 0.20, respectively. *P* values are represented by ns, $P > 0.05$; ****$P < 0.0001$. (*C*–*F*) DFS plots showing the distribution of the rupture forces as a function of their LR measured between reovirus and JAM-A, with binding frequency plotted as function of contact time in the inset for engineered mutants (*C*) Head (N = 2,166 data points), (*D*) HeadΔSA (N = 4,317 data points), (*E*) Body (N = 3,005 data points), and (*F*) Tail (N = 4,909 data points). In the DFS plots, the solid line represents the fit of the data with the BE fit (for simple ligand–receptor bond). In the binding frequency plots (*Insets*), data points were fitted using a least-squares fit of a monoexponential decay. The error bars indicate SD. All data are representative of at least n = 3 independent experiments.

and single-rupture events (*SI Appendix*, Figs. S7 and S8) were analyzed using the BE model. All the four mutants displayed lower conformational variability in the bound state, as indicated by ≈twofold reduction of the x_u (*SI Appendix*, Table S1). In addition, the two head mutants (Head and HeadΔSA) exhibited the lowest k_{off} values, suggesting a stabilized bound state. Further comparison of the different fits revealed that all the four mutants, as well as ISVPs, significantly differ from WT T1L VPs (*SI Appendix*, Fig. S9), suggesting that formation of an extended σ1 conformer influences stability of the σ1–JAM-A complex. We also analyzed association rates (Fig. 3 *C–F*, *Insets*) and observed stabilization of the bound state, marked by a higher k_{on} for both the Head and HeadΔSA mutants (*SI Appendix*, Table S1). Finally, the affinity constant K_D, calculated from the respective k_{on} and k_{off} values, showed that Head and HeadΔSA have higher affinity for JAM-A relative to the Tail and Body mutants, which showed no significant changes relative to WT T1L VPs.

Collectively, results obtained using the σ1 disulfide mutants indicate that cross-linking of the head domain leads to a more stable bound state (lower K_D), primarily attributable to a higher association rate. On the contrary, all mutants exhibit, in the binding free-energy landscape, an energy barrier at a lower distance, indicating that the bound state is capable of accommodating fewer conformational states (*SI Appendix*, Fig. S10). Furthermore, this barrier may represent the distance the molecule must span between bound and unbound states and indicate its complex mechanical compliance. High values suggest a soft mechanical response, while low values imply a brittle complex. In a more physiologically relevant context, these findings suggest that head domain cross-linking, while improving stability of the complex, yields poor complex compliance.

Deciphering the Influence of σ1 Conformational Change on Cell Attachment. To determine the influence of σ1 conformational change on attachment to cells, we probed the binding of T1L variants to JAM-A on living Lec2 cells. Lec2 cells were selected for these experiments, as these cells do not express JAM-A and display little sialic acid on the cell surface, leading to poor reovirus binding, as confirmed by a cell-binding assay (*SI Appendix*, Fig. S11) (32, 33). Lec2 cells that stably express JAM-A (Lec2 JAM-A) bind reovirus more efficiently. For the AFM experiments, we cocultured Lec2 JAM-A cells and Lec2 cells that express the fluorescent construct (actin:mCherry, H2B:GFP), allowing us to distinguish the two cell lines (Fig. 4*A*). Using FD-based AFM (19), we simultaneously collected FD curves (Fig. 4*B*) and height and adhesion maps in an area containing adjacent Lec2 JAM-A and Lec2 cells (Fig. 4 *D–F*). Using this approach, we were able to probe both cell types with the same virion to allow direct comparison of the BFs (Fig. 4*C*) and distribution of binding events (Fig. 4 *D–F*).

For WT T1L VPs and the mutants, the BFs were extracted by pixel counting on the adhesion maps (Fig. 4*C*). For each condition, the BF for Lec2 cells was significantly lower than that for Lec2 JAM-A cells, confirming that most of the probed interactions on Lec2 JAM-A cells are attributable to JAM-A binding. As an additional control, JAM-A Ab was injected to block interactions with σ1, which led to a significant decrease in the BFs for Lec2 JAM-A cells (*SI Appendix*, Figs. S12 and S13). Overall, the BF of T1L VPs and the Head mutant were slightly higher than those of the other mutants.

To further investigate the capacity of these virus strains to bind JAM-A expressed on living cells, we extracted the binding strength/LR pairs for each specific adhesive event and overlaid these data points on the DFS plots previously obtained in experiments using model surfaces (Fig. 5). For all the five viruses (WT T1L VPs and the four mutants), the extracted forces were in the 50 to 500 pN range, corresponding to single- and multiple-bond rupture events. We therefore used the Williams–Evans model (Fig. 5 *B–F*, dashed lines) (34) to predict the forces associated with the rupture of simultaneous uncorrelated bonds that are established in parallel. The overlay of the rupture forces data recorded from experiments using living cells, as well as the mean rupture forces extracted from the histograms fitted with multiple Gaussian peak distribution (Fig. 5 *B–F*, on the side), revealed agreement between the force of the single bond extracted using living cells and those obtained in experiments using purified JAM-A. Of note, the predictions for multiple interactions coincide well in the case of WT T1L VPs and the Body and Tail mutants, but these predictions fail to predict the extracted forces for both the Head and HeadΔSA mutants. Thus, cross-linking of the tail and body domains appears to diminish the capacity to form multivalent bonds, with the vast majority of rupture bonds being single-bond rupture events. These results indicate that in virus attachment to cells, which more faithfully reflects physiological conditions, cross-linking of the σ1 head domain leads to weaker interaction strength than predicted for double or triple bonds. Furthermore, this observation suggests that under polyvalent binding conditions, the most stable bound states are not reached for the head mutants. However, single-bond rupture forces for the head mutants match well with those obtained using model surfaces and, when compared with WT T1L, triple-bond forces appear to be slightly higher for Head and HeadΔSA. This finding highlights an antagonism between higher affinity of σ1 for JAM-A and the flexibility of individual σ1 domains, which influences the stability of multimeric complex formation. The capacity to modulate host cell attachment could be useful in the improvement of oncolytic vectors, as has been done for different strains of adenovirus (35).

T1L σ1 Mutations Affect Virus Diffusion and Uptake into Cells. Since σ1 flexibility appears to influence the formation of multivalent bonds with JAM-A, we investigated whether cross-linking the head domain also influences virus binding to and infection of CHO JAM-A cells (Fig. 6*A*). To quantify virus binding, cells were adsorbed with WT T1L, Head, or HeadΔSA at 4 °C to allow attachment but not cell entry. Levels of bound WT, Head, and HeadΔSA virions suggest that cross-linking the σ1 head domain leads to diminished binding to the cell surface. While Head binding is ~18-fold lower than that of WT, HeadΔSA binding is ~2,000-fold lower than that of WT. To quantify the infectivity of WT T1L and the head mutants, cells were incubated with virions at 37 °C, and virus titers were determined at 4 h postadsorption to allow internalization but not replication and assembly of new virus particles. After standardizing to input virus titers, we observed ~threefold higher infectivity of the Head mutant relative to WT T1L, whereas HeadΔSA displayed ~50-fold lower infectivity relative to T1L. Together, these results highlight the importance of σ1 flexibility in binding to host cells, as the rigidity caused by cross-linking the σ1 head domain impairs the capacity of the virion to bind cell-surface receptors. However, the interesting increase in infection efficiency for the Head mutant suggests that a higher affinity for JAM-A provides an advantage to productively infect cells.

Because there is a close relationship between the capacity of viruses to attach to cellular receptors, as well as to diffuse and explore cell surfaces, we determined the diffusion behavior of different viral strains using confocal microscopy and SPT analysis (Fig. 6*D*). Virions fluorescently labeled with Atto488 (mutants) or Alexa488 (WT T1L VP) were injected in a culture with Lec2 JAM-A (Fig. 6 *F–G*) or Lec2 cells (*SI Appendix*, Fig. S14). Stationary virions or tracks of virions diffusing across the cell surface were selected and used to calculate the mean diffusion speed from experiments using

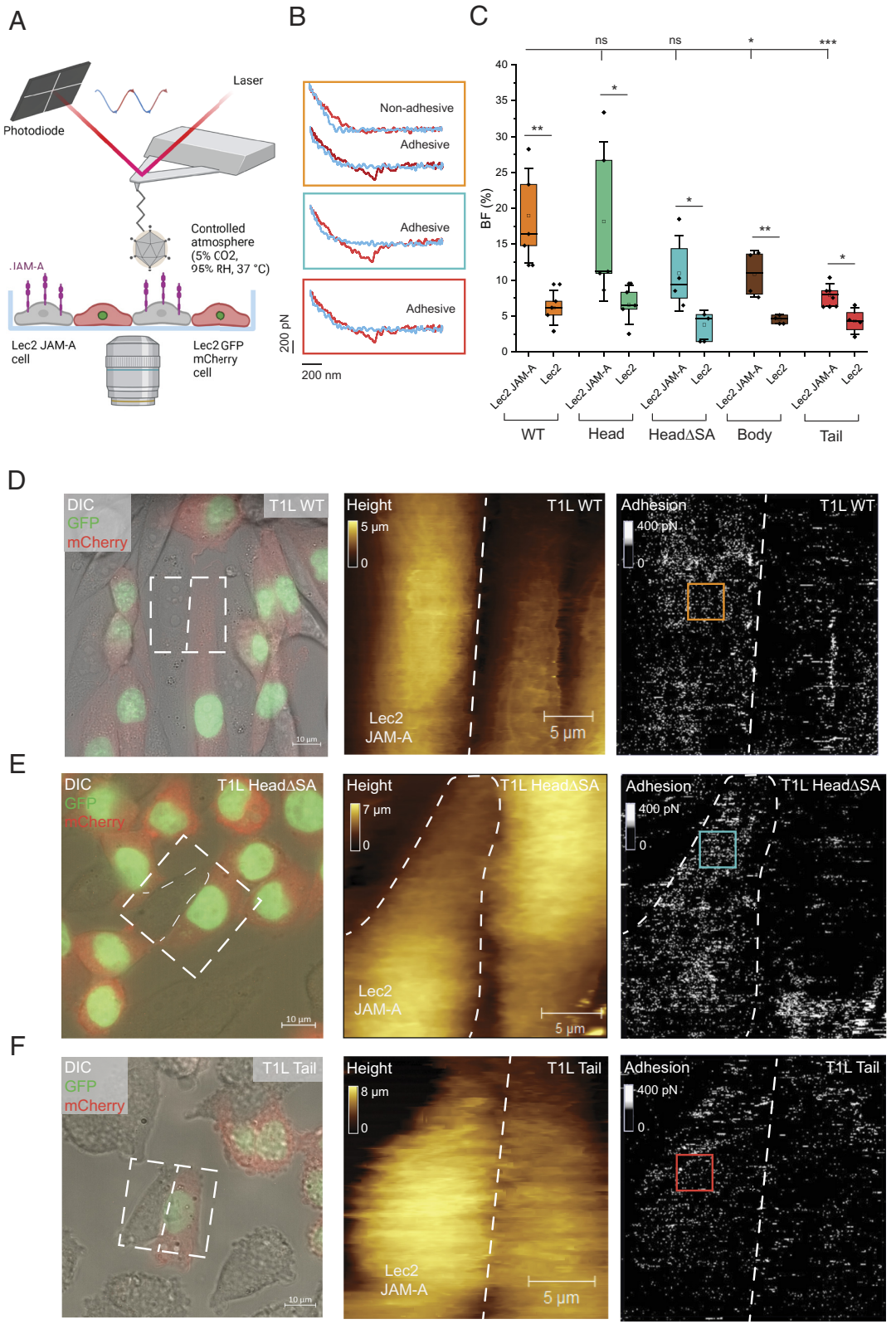

Fig. 4. Probing T1L binding to JAM-A on living cells. (*A*) Combined optical microscopy and FD-based AFM of T1L VPs (tethered to the AFM tip) binding to Lec2 JAM-A or Lec2 cells in coculture. (*B*) Representative FD curves recorded by cyclically approaching and retracting the tip to and from the cell's surface, using Lec2 JAM-A cells. FD curves showing nonadhesion or specific adhesion events with either T1L WT, HeadΔSA, or Tail VPs. (*C*) Box plot of the BF between virions and Lec2 or Lec2 JAM-A cells. The horizontal line within the box indicates the median, boundaries of the box indicate the 25th and 75th percentiles, and the whiskers indicate the SD. Statistical significance was determined for the log-transformed BF by two-sample *t* test. *P* values for the comparison between WT T1L VPs and Head, HeadΔSA, Body, or Tail mutants are 0.65447, 0.06227, 0.04274, and 0.00063, respectively. *P* values are represented by ns, $P > 0.05$; *$P < 0.05$; **$P < 0.01$; ***$P < 0.001$. (*D*–*F*) Overlay of DIC and fluorescence channel with the AFM-scanned area outlined. FD-based AFM topography image and the corresponding adhesion map collected from the specified scanned area for T1L WT (*D*), HeadΔSA (*E*), and Tail (*F*) VPs. Cartoon in panel *A* was created in BioRender.com.

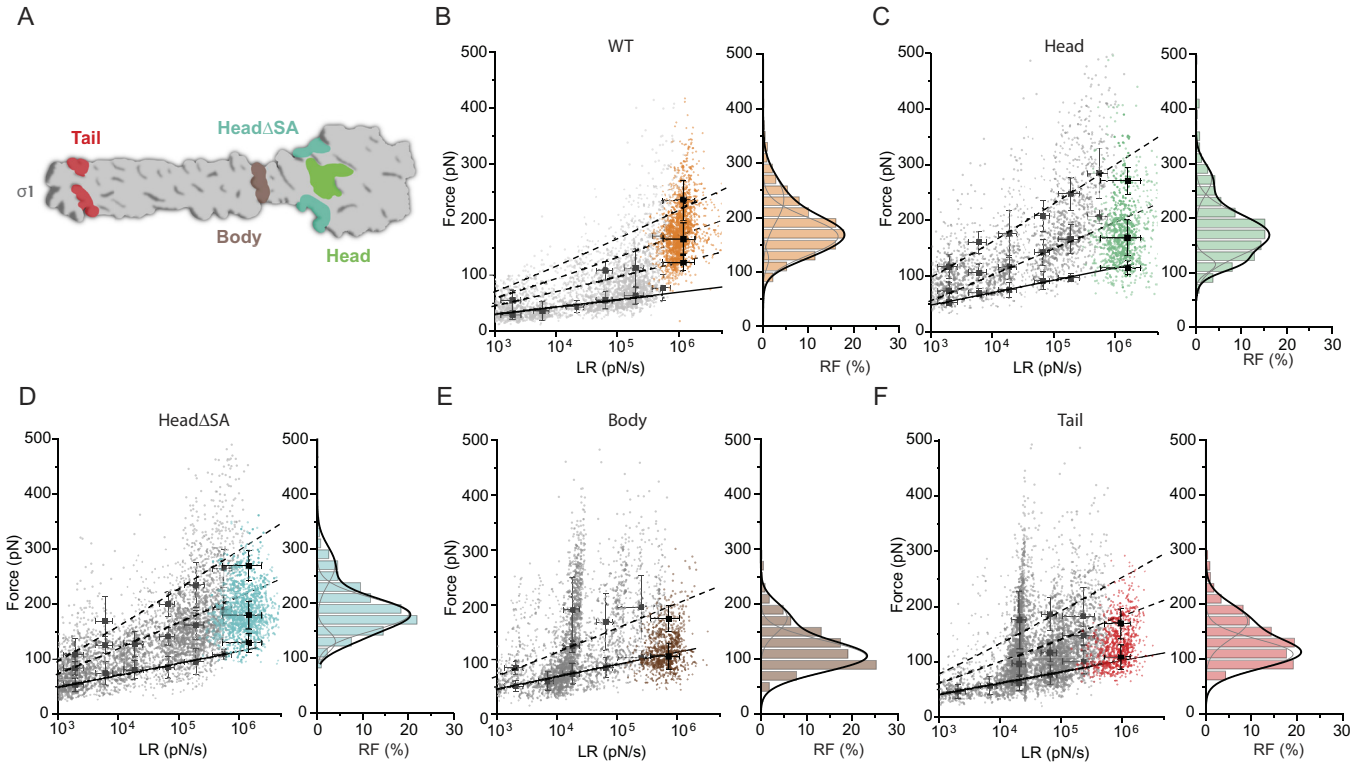

Fig. 5. Forces involved in the interaction of virions and JAM-A on living cells. (*A*) Space-filling model of σ1 showing locations of engineered cysteine mutations in the tail, body, and head domains. (*B–F*) DFS plots comparing data for virions and JAM-A on model surfaces (gray dots) with overlaid data points from binding experiments using living cells (colored dots) for (*B*) WT T1L (N = 1,546 data points, orange), (*C*) Head (N = 961 data points, green), (*D*) HeadΔSA (N = 1,227 data points, light blue), (*E*) Body (N = 857 data points, brown), and (*F*) Tail (N = 809 data points, red). On the side are shown the respective histograms of the force distribution observed using cells and their relative frequency (RF) fitted with a multipeak Gaussian distribution.

both cell lines (Fig. 6*E* and *SI Appendix*, Fig. S14). Mean diffusion speeds observed for WT T1L VPs on cells expressing JAM-A were within 0.01 μm s^{-1} to 0.4 μm s^{-1} (Fig. 6*E*), consistent with heterogeneous behavior ranging from stable attachment to cell receptor–directed diffusion (36). The Head mutant displayed a slightly lower mean diffusion speed relative to WT T1L VPs, while the Body and Tail mutants displayed increased mean speeds. The Head mutant showed very small dispersion of the data with low speeds, suggesting that a vast majority of the virions are immobile. In contrast, the other mutants diffuse faster than WT T1L VPs, possibly due to lower affinity for JAM-A (Fig. 4) or diminished capacity to establish multivalent bonds (Fig. 5). The reduced diffusion observed for the Head mutants also could be attributable to a more extended σ1 conformer, which might prevent virions from diffusing through the crowded glycoprotein matrix at the cell surface.

To test this hypothesis, we evaluated the hydrodynamic radius of WT and mutant virions, tracking the virions undergoing Brownian motion in a sucrose solution (*SI Appendix*, Fig. S15). We observed a similar radius for all strains, between ~40 and 50 nm, in good agreement with previous data (17), as well as previous dynamic light scattering studies of WT T1L VPs and the mutants (31). This observation suggests that the σ1 mutations do not influence the rate of free VP diffusion. Overall, the SPT experiments reveal that the T1L mutants diffuse at different speeds only when interacting with the cell membrane, possibly due to a change in σ1 affinity for JAM-A and the capacity to establish multivalent bonds. Results from virus diffusion and infectivity assays suggest that after encountering and binding to the receptor, Head mutant tends to remain bound and trigger internalization with high efficiency. Thus, we elucidate an intricate σ1–JAM-A mechanism in which flexibility and affinity of the binding partners can be modulated to affect binding and infection of VPs.

Conclusions

The study of the early steps of reovirus binding to cells is of major importance in our understanding of how we can manipulate virus binding and consequent infectivity. Current knowledge of the molecular mechanisms of reovirus binding and entry relies mainly on ensemble techniques that monitor either virus attachment or infectivity as well as high-resolution structural data of the molecular complexes associated with those steps. These data have two major limitations: the static nature of the molecular views and the averaging of observations for large viral populations. Both types of measurements fail to reflect the stochastic nature of individual behaviors and limit the information that can be extracted, including fine molecular changes. In this study, we used AFM, which allows investigation of the dynamics of virus binding at the single-virus particle level and even the single-bond level, thus yielding kinetic and thermodynamic parameters of the established interactions. We used AFM in combination with purified receptor or with whole cells, which are complex biological interaction surfaces. However, this technique also has limitations. Binding is monitored for very short intervals, and bonds are artificially broken under the effect of an external charge after a specified contact time. Although it provides a robust quantitative analysis of early interactions established at the cell surface, the force analysis is, therefore, conducted out of equilibrium. The cell lines used were engineered to express JAM-A and in some cases do not express glycans. This strategy allowed interaction data to be compared for an otherwise identical non-JAM-A-expressing cell line but may be less biologically relevant than using cell types that naturally express the reovirus receptors. We also used SMD to better understand differences in affinity between JAM-A and GM2-liganded or unliganded σ1. While this approach provides insights into the

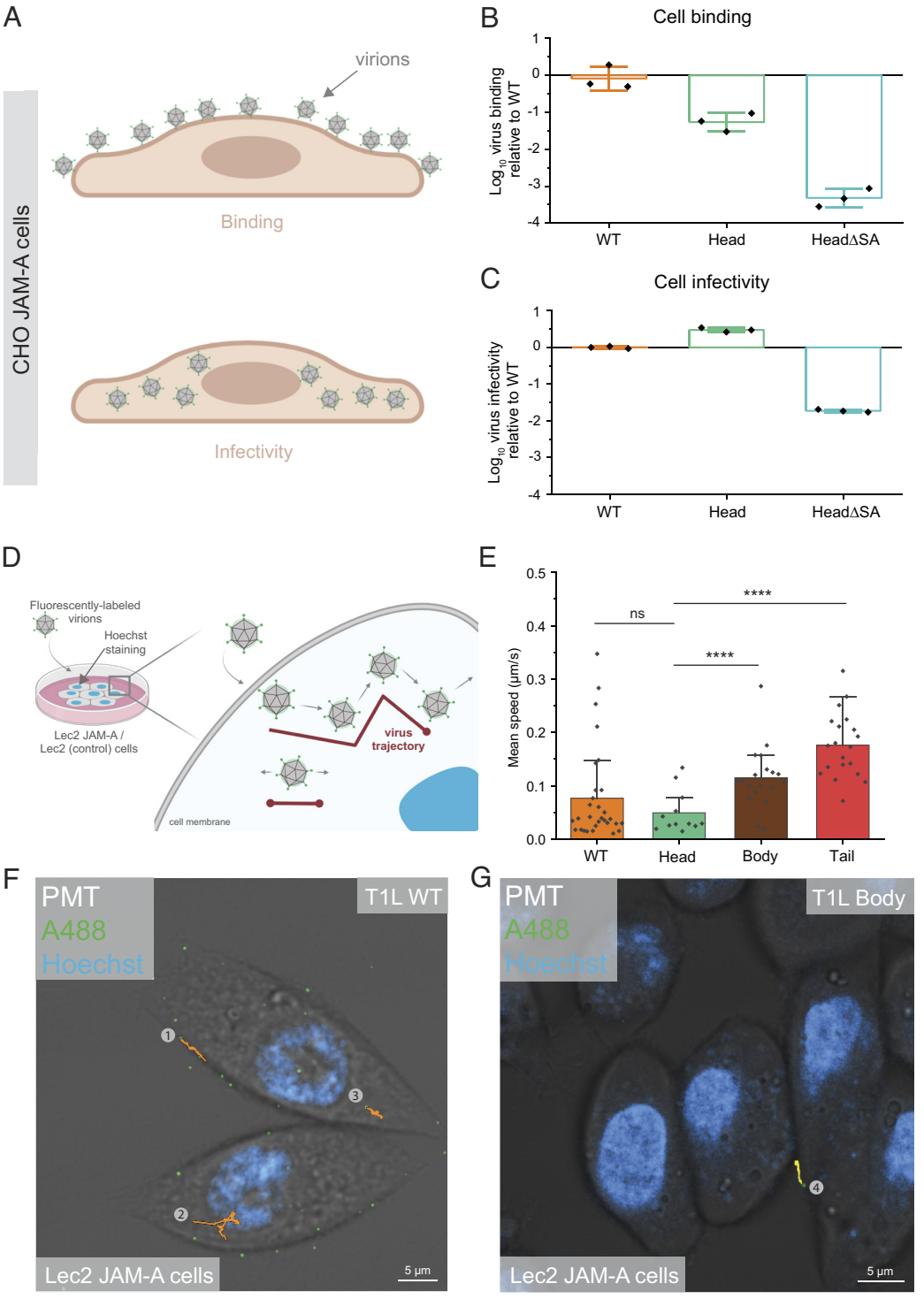

Fig. 6. Binding, infectivity, and diffusion of T1L virions on living cells. (*A*) Schematic of cell binding (conducted at 4 °C) and infectivity assays (conducted at 37 °C) using CHO–JAM-A cells. (*B* and *C*) WT, Head, or HeadΔSA mutants (10^4 particles/cell) were incubated with CHO–JAM-A cells at 4 °C for 1 h, and binding relative to WT T1L was determined by quantitative immunoblotting (*B*) or at 37 °C for 4 h, and infectivity relative to WT T1L was quantified by plaque assay (*C*). Results are expressed in Log_{10} of virus binding or infectivity relative to WT T1L for three experiments. Bars indicate the mean, and error bars represent SD. (*D*) Representation of an SPT experiment. Virions of WT T1L, Head, Body, or Tail were labeled with Alexa or Atto 488 and adsorbed to Lec2 JAM-A cells. Tracks of particles undergoing lateral particle diffusion or stationary were collected. (*E*) Bar graphs of mean diffusion speed calculated for WT, Head, Body, and Tail virions following adsorption to Lec2 JAM-A cells. Tracks of at least 10 virions were collected for each condition. The box indicates the mean, and whiskers indicate the SD. Statistical significance was determined for the mean diffusion speed by Mann–Whitney *U* test. *P* values for the comparison between Head and WT T1L, Body, or Tail are 0.1997, 2.338×10^{-7}, and 3.489×10^{-9}, respectively. *P* values are represented by ns, $P > 0.05$; ****$P < 0.0001$. (*F* and *G*) Overlay of images of transmitted light photomultiplier imaging (T-PMT), Hoechst33342 (blue; nucleus of the cells), and Alexa/Atto 488 (green; virions) signals from a time series collected using Lec2 JAM-A cells, where WT T1L VP (tracks #1-3) (*F*) or Body (track #4) (*G*) was added. Examples of tracks belonging to virions interacting with the cell membrane for WT T1L (orange) and Body (yellow) were superimposed. Cartoons in panels *A* and *D* were created in BioRender.com.

dynamics of the interaction and is supported by AFM and other assay data, it is computational data based on structural models, and it does not predict complex interactions at the cell surface, where multiple glycans and JAM-A molecules may engage a σ1 trimer simultaneously. Although no individual approach is without fault, combining data from multiple different approaches can

provide a more complete understanding of virus–receptor interaction dynamics.

In the first part of this study, we used AFM to probe interactions between reovirus T1L and proteinaceous cell-surface receptor JAM-A. We discovered that, in vitro, ISVPs display only slightly enhanced binding kinetics for JAM-A relative to WT VPs, while the addition of GM2 glycans leads to a twofold increase in affinity for VPs for JAM-A as well as a slight increase for ISVPs. To better understand the molecular mechanisms underlying the stabilization of the complex in the presence of GM2 glycan, we conducted SMD simulations, which provided evidence for a mechanism in which GM2 stabilizes the σ1–JAM-A complex for reovirus T1L. Although for both VPs and ISVPs the affinity of reovirus–JAM-A binding is increased, the mechanism for T1L differs from that observed for T3D, for which the higher affinity was directly linked to a conformational change in σ1. These different behaviors can be linked to the positions of sialylglycan-binding sites on the σ1 protein that differ between the two serotypes. In addition, we observed that cross-linking of the σ1 head domains also leads to a higher affinity for JAM-A, reminiscent of the behavior previously observed for T3D (14).

Together, these results shed light on the dynamics and cooperativity of interactions established by reovirus with the cell-surface receptors. After the VP lands on the cell surface, both glycan engagement and conformational changes in the viral capsid can lead to an increase in affinity for cell-entry receptors. These results, acquired by single-molecule techniques, indicate the importance of σ1 flexibility in the engagement of JAM-A at the cell surface and were confirmed by macroscopic assays, such as binding and infectivity tests, as well as SPT. We found that cross-linking the σ1 head domain results in enhanced infectivity of VPs, which agrees with SPT data showing lower diffusion speeds on the cell membrane for the same mutant.

This work deepens the knowledge obtained from previous studies and highlights that viral attachment factors play a key role in the initial stages of binding. During evolution, different viruses or different virus serotypes have selected different strategies to exploit the early foothold established between virus and cell-surface glycans. Understanding this mechanism opens possibilities to more precisely control the binding and entry of reoviruses, opening therapeutic opportunities.

Methods

Culture of Cell Lines. Lec2 and CHO-K1 (CHO) cells were purchased from ATCC (CRL-1736, CCL-61). Lec2 and CHO cells stably expressing actin-mCherry and H2B-GFP and CHO and Lec2 cells stabling expressing JAM-A were previously established (14). Lec2 cells were cultured in MEM α nucleosides medium (Gibco, the Netherlands). CHO cells were cultured in Ham's F12 medium (Sigma-Aldrich, United Kingdom). Media were supplemented with 10% FBS (Gibco, USA), 100 units.mL^{-1} penicillin, 100 μg mL^{-1} streptomycin (Sigma-Aldrich, USA), 2 mM L-Glutamine (Sigma-Aldrich, USA) and 100 μg mL^{-1} Normocin (InvivoGen, France). Spinner-adapted L929 fibroblasts (L cells) were grown in suspension culture in Joklik's minimum essential medium (US Biological) supplemented with 5% FBS (Gibco, USA), 2 mM l-glutamine (Corning, USA), 100 U/mL penicillin, 100 μg mL^{-1} streptomycin (Corning, USA), and 25 ng mL^{-1} amphotericin B (Corning, USA). All cells were grown at 37 °C in a humidified atmosphere with 5% CO_2.

Viruses. Laboratory stocks of parental reovirus strain rsT1L and σ1 cysteine mutants were engineered using plasmid-based reverse genetics, as described (31). Viral titers were determined by plaque assay using L cells, as described (37). VPs were purified from infected L cells by deoxycholate permeabilization, Vertrel XF (DuPont) extraction, and CsCl gradient centrifugation, as described (18). ISVPs were prepared by treatment of purified VPs with chymotrypsin (Sigma-Aldrich, USA) (38).

Labeling of the Reovirus with Fluorescent Dye. Reovirus virions were labeled with Atto 488 succinimidyl ester (Atto 488-NHS; ATTO-TEC, Germany) as described (39, 40). Labeled VPs were dialyzed against PBS (Sigma-Aldrich, United Kingdom) buffer at 4 °C using Slide-A-Lyzer™ MINI Dialysis Device Kit, 10 K MWCO, 0.1 mL (Fisher Scientific, IL, USA). Another dialysis step followed, using a dialysis tubing cellulose membrane (Sigma-Aldrich, MO, USA) with a molecular weight cutoff of 14,000 g mol^{-1}, by immersing it in PBS overnight. Finally, an Amicon Ultra-0.5 centrifugal filter unit (Millipore, Germany) was used to collect the VPs, which were stored at 4 °C until further use.

Functionalization of AFM Tips. AFM tips were functionalized with APTES, followed by Ald-Ph-PEG_{24}-NHS linker and, lastly, VPs, using previously described protocols (41, 42). The functionalized tips were placed in individual wells of a multiwell plate, in 2 mL of virus buffer. The tips were stored at 4 °C until further use.

Preparation of JAM-A-Coated Model Surfaces. His-tagged JAM-A protein (0.1 mg mL^{-1}; BioConnect, Canada) was immobilized using NTA-His_6 binding chemistry, as previously described (43). The surfaces were stored at 4 °C until further use, always keeping the surfaces hydrated.

FD-Based AFM on Model Surfaces. Force distance (FD)–based AFM experiments were performed in PBS, using virus-functionalized MSCT-D probes (Bruker, Germany). Cantilever spring constants were calculated using thermal tune method (44), with values within the range of 0.023 to 0.043 N m^{-1}. For all experiments, the ramp size was set to 500 nm, the approach velocity to 1 μm s^{-1}, and the maximum force to 500 pN. DFS experiments were conducted with no surface delay and by varying the retraction velocities, set to 0.1, 0.2, 1, 5, 10, and 20 μm s^{-1}. k_on measurements were conducted by varying the hold times (0, 50, 100, 150, 250, 500, and 1,000 ms).

Surface blocking was conducted as an independent negative control by adding JAM-A antibody (Sigma-Aldrich, Germany) at a concentration of 100 μg mL^{-1}.

Selected FD curves were fitted with the worm-like chain model for polymer extension (45). Regarding DFS experiments, LRs were determined using the slope of the force–time curves and rupture forces were extracted (19, 46). For kinetic on-rate analysis, the BF was determined for the different hold times. Those data were fitted and K_D calculated as described (47).

MD Simulations and Analyses. The tridimensional structure of the complex T1L–σ1–JAM-A coupled with GM2, for simplicity called σ1(GM2)–JAM-A, was modeled with Modeller v.10.1 (48), using as templates the crystallographic structures of T1L–σ1 in complex with GM2 (PDB id 4gu3) (12) and T1L–σ1 in complex with JAM-A (PDB id 4odb) (16). The system was initially built with GM2 molecules, which were subsequently removed from the model to create the σ1–JAM-A system. Parameters for glycan molecules and model structure preparation were obtained through the CHARMM-GUI web interface (49). The complex was solvated using TIP3 water model (50) and the total charge neutralized using NaCl 0.15 mol L^{-1} ion concentration. Simulation parameters were obtained from QwikMD (51), and all molecular dynamics (MD) simulations were conducted employing the NAMD three package (25). Simulations were carried out at the local NVIDIA DGX-A100–based cluster nodes at Auburn University. The CHARMM36 force field (52) was used to describe the system, and the simulations were conducted under periodic boundary conditions. A distance cutoff of 12.0 Å was applied to short-range nonbonded interactions, whereas long-range electrostatic interactions were treated using the particle-mesh Ewald method (53). Before the SMD simulations, the systems were minimized and equilibrated in three steps: i) energy minimization for 5,000 steps followed by a short 1.0 ns MD using an NVT ensemble, with restraints (100 kcal mol^{-1} Å^2) on backbone and sugar atoms (when present); ii) 1.0 ns MD in an NpT ensemble with restraints (10 kcal mol^{-1} Å^2) on backbone and sugar atoms (when present); iii) unrestrained 1 ns MD. The temperature was maintained at 300 K using Langevin dynamics for temperature and pressure coupling, the latter kept at 1 bar for NpT MD simulations. The time step of integration was chosen to be 4 fs for all SMD production simulations conducted and 2 fs for all equilibration runs. SMD simulations were conducted in 40 replicas for each system, with a total of 60 ns each replica. In total, nearly 5.0 μs of MD was conducted. During SMD, the N-terminal residue of each T1L monomer was anchored, while the C-terminal residue of one of the JAM-A molecules was pulled at a constant speed of 2.5 × 10^{-04} nm ps^{-1} with a 0.144 kcal mol^{-1} Å^2 spring constant.

The PMF was calculated over the dissociation path obtained from the SMD simulations, considering the distance between the anchor and pulling points

as the reaction coordinates. The method uses the Jarzynski's equality to connect nonequilibrium properties (SMD simulations) with equilibrium properties. The PMF was estimated by accumulating the logarithm of the exponential average of the work over all replicas (28).

The most probable LR for the rupture events was determined with a kernel density estimator (KDE) with the bandwidth chosen through the Silverman estimator (54). The LR was used to fit the rupture force histograms with the BE model to determine the most probable rupture force, the distance to the transition state $\Delta x0$, the natural off-rate at zero force $koff_0$, and the energy barrier ΔG^{++} in units of k_BT at T = 300 K.

Mean correlation between σ1–JAM-A interface residues was calculated using dynamical network analysis (29) and VMD (55). In dynamical network analysis, a network is defined as a set of nodes that represent amino acid residues, and the node's position is mapped to that of the residue's α-carbon. Edges connect pairs of nodes if their corresponding residues are in contact, and two nonconsecutive residues are said to be in contact if they are within 4.5 Å of each other for at least 75% of analyzed frames. The interface residues between σ1 and JAM-A were defined in a radius of 10 Å between nodes in each molecule. The analysis was carried out 5 ns before and 2 ns after the first peak force.

The intermolecular surface contact area (Å^2) was calculated using in-house scripts based on Connolly's solvent accessible surface algorithm (56).

All charts were generated using in-house python scripts. The protein image was rendered using VMD.

FD-Based AFM and Fluorescence Microscopy on Living Cells. AFM (Bioscope Resolve, Bruker, Santa Barbara, CA, USA), operated in the PeakForce QNM mode (NanoScope software v9.2), coupled to an inverted epifluorescence microscope (Zeiss Observer Z.1, Zeiss, A 40× oil objective (NA = 0.95) was used. Cells were kept in media and a cell-culture chamber was used to maintain temperature at 37 °C ± 1 °C, with 5% CO_2 and 95% relative humidity. PFQNM-LC precalibrated cantilevers (Bruker, Santa Barbara, CA, USA) were used and their sensitivity was calculated through thermal noise method. The cantilevers were oscillated at 0.25 kHz in PeakForce tapping mode, with an amplitude of 750 nm, a set-point of 500 pN, and a scan frequency of 0.125 Hz. AFM images and FD curves were analyzed with NanoScope analysis software (v1.7, Bruker), Origin software (OriginPro 2021, 9.8.0.200), ImageJ (v1.52e), and Gwyddion (version 2.58). As control experiments, JAM-A antibody was added at 50 μg mL^{-1} (Sigma-Aldrich, Germany).

Cell-Binding Assay. Virus binding to cells was quantified as described (31). Lec2, Lec2 JAM-A, or CHO JAM-A cells (5×10^5) were aliquoted into Eppendorf tubes on ice. Dilutions of purified WT VP, WT VP + 1 mM GM2, or ISVP (10^4 particles/cell) were prepared in cold medium. In the case of Lec2 and Lec2 JAM-A cells, dilutions of 5×10^4 (5×) and 2.5×10^5 (25×) particles/cell also were prepared in cold medium. Cells were pelleted and adsorbed with virus, medium (mock), or medium + 1 mM GM2 at 4 °C for 1 h. Following adsorption, the cells were pelleted and washed twice prior to addition of radioimmunoprecipitation assay (RIPA) buffer supplemented with 1 mM phenylmethylsulphonyl fluoride (PMSF). Samples were boiled with SDS sample buffer and resolved on a 10% Mini-Protean TGX precast protein gel (Bio-Rad). Proteins were transferred to nitrocellulose membranes, which were blocked in Pierce protein-free (PBS) blocking buffer, then incubated with 1:2,000 diluted mouse monoclonal anti-GAPDH (Invitrogen) and 1:500 diluted rabbit polyclonal anti-reovirus serum. Membranes were washed in PBS + 0.1% Tween20 and incubated with anti-rabbit IRDye680LT and anti-mouse IRDye800CW antibodies (LI-COR) diluted 1:15,000 in PBS + 0.1% Tween20 + 5% nonfat dry milk. After washing, the membranes were scanned using a ChemicDoc MP imaging system (BIO-RAD). Protein band intensity was quantified using Image Lab 6.1 (BIO-RAD) and normalized to that of WT VP.

Cell Infectivity Assay. To quantify the infectivity of bound virus, dilutions of purified WT VP, Head VP, or Head ΔSA VP (10^4 particles/cell) were prepared in cold medium. CHO JAM-A cells (5×10^5) were aliquoted into Eppendorf tubes on ice and adsorbed with virus at 4 °C for 1 h. Following adsorption, cells were pelleted and washed twice. RIPA buffer was added to cells in half of the samples, and they were processed as described above in the cell-binding assay, to quantify virus adherence to the cell surface. Cells in the other half of samples were resuspended in prewarmed medium and incubated at 37 °C for 4 h to permit infection but not a complete replication cycle. The cells were then lysed by two rounds of freezing at −80 °C and thawing to release virus, and virus titer in the samples was determined by plaque assay on L cells. Sample titer was adjusted based on input titer for each virus. Protein band intensity and infectivity titers each were quantified and normalized to those of WT VP.

SPT. In all experiments, tracks of reovirus virions labeled with Atto 488 or Alexa 488 were collected. Lec2 JAM-A and Lec2 cells were kept in MEM α, nucleoside medium (Gibco). Cells were incubated at 4 °C for 30 min prior to the experiment, and DNA was stained with Hoechst33342 (ThermoFisher, USA) as per supplier protocol. Virions of WT T1L, Head, Body, and Tail were added to the samples, and tracks of particles were collected. A Zeiss 980 confocal laser-scanning microscope (Zeiss GmbH, Germany) was used to acquire time series and Z-stack images. Images were processed using Zen Blue software (version 3.2, Zeiss, Germany), and time series images were analyzed with ImageJ (v1.52e). Individual viruses were tracked using the TrackMate plugin, and the trajectory data were exported to Microsoft Excel for further analysis. Behaviors of at least 10 virions per sample were analyzed by extracting their diffusion rate. Population statistics were graphed using Origin software (OriginPro 2021, 9.8.0.200). In order to assess the free diffusion rate of the reovirus T1L WT and mutants, virions were added to a ~13.3% or 16% sucrose solution. The retrieved diffusion speeds were used to estimate the hydrodynamic radius through input into the Stokes–Einstein equation. All sucrose experiments were conducted at RT.

Statistical Analysis. JMP® Statistical Software (JMP® Pro 16.0.0) and https://www.statskingdom.com/ were used to conduct statistical tests. Statistical significance of BF values was assessed by conducting two-sample *t* tests. To achieve a normal distribution of the results, a log 10 of the BF was used for statistical analysis of the data from experiments with living cells. Statistical significance of mean diffusion speed values, which did not follow a normal distribution, was assessed by conducting Mann–Whitney *U* tests.

Data, Materials, and Software Availability. All study data are included in the article and/or *SI Appendix*.

ACKNOWLEDGMENTS. This work was supported by the Université catholique de Louvain and the Fonds National de la Recherche Scientifique (FRS-FNRS). This project also received funding from the FNRS-Welbio (Grant # CR-2019S-01) and the NIH (R01 AI155646 to K.M.O. and R01 AI174526 to T.S.D.). The funders had no role in study design, data collection, and analysis; decision to publish; or preparation of the manuscript. M.K. and J.S. are postdoctoral researchers, and D.A. is a research associate at the FNRS. Additional support was provided by the NSF under Grant MCB-2143787 (CAREER: In Silico Single-Molecule Force Spectroscopy). We thank Auburn University and the College of Sciences and Mathematics for the computational resources provided to Dr. Bernardi.

Author affiliations: [a]Louvain Institute of Biomolecular Science and Technology, NanoBiophysics lab, Université catholique de Louvain, 1348 Louvain-la-Neuve, Belgium; [b]Leibniz Institute for Food Systems Biology at the Technical University of Munich, 85354 Freising, Germany; [c]Department of Physics, Auburn University, Auburn, AL 36849; [d]Department of Pathology, Microbiology, and Immunology, Vanderbilt University Medical Center, 37232 Nashville, TN; [e]Department of Pediatrics, University of Pittsburgh School of Medicine, Pittsburgh, PA 15213; [f]Department of Microbiology and Molecular Genetics, University of Pittsburgh School of Medicine, Pittsburgh, PA 15213; [g]Institute of Infection, Inflammation, and Immunity, University of Pittsburgh Medical Center, Children's Hospital of Pittsburgh, Pittsburgh, PA 15213; [h]Department of Pediatrics, Division of Infectious Diseases, Vanderbilt University Medical Center, Nashville, TN 37232; and [i]Walloon Excellence in Life sciences and Biotechnology, Walloon Excellence Research Institute, 1300 Wavre, Belgium

1. K. M. Guglielmi, E. M. Johnson, T. Stehle, T. S. Dermody, Attachment and cell entry of mammalian orthoreovirus. *Curr. Top. Microbiol. Immunol.* **309**, 1–38 (2006).
2. R. Bouziat *et al.*, Reovirus infection triggers inflammatory responses to dietary antigens and development of celiac disease. *Science* **356**, 44–50 (2017).
3. M. B. Phillips *et al.*, Current understanding of reovirus oncolysis mechanisms. *Oncolytic virother.* **7**, 53 (2018).
4. D. Clements, E. Helson, S. A. Gujar, P. W. Lee, Reovirus in cancer therapy: An evidence-based review. *Oncolytic Virother.* **3**, 69 (2014).
5. K. Kelly *et al.*, Reovirus-based therapy for cancer. *Exp. Opin. Biol. Ther.* **9**, 817–830 (2009).
6. M. Marsh, A. Helenius, Virus entry: Open sesame. *Cell* **124**, 729–740 (2006).
7. M. Delguste *et al.*, Multivalent binding of herpesvirus to living cells is tightly regulated during infection. *Sci. Adv.* **4**, eaat1273 (2018).

8. M. Koehler, M. Delguste, C. Sieben, L. Gillet, D. Alsteens, Initial step of virus entry: Virion binding to cell-surface glycans. *Annu. Rev. Virol.* **7**, 143–165 (2020).
9. D. M. Reiter *et al.*, Crystal structure of reovirus attachment protein σ1 in complex with sialylated oligosaccharides. *PLoS Pathog.* **7**, e1002166 (2011).
10. J. D. Chappell, A. E. Prota, T. S. Dermody, T. Stehle, Crystal structure of reovirus attachment protein σ1 reveals evolutionary relationship to adenovirus fiber. *EMBO J.* **21**, 1–11 (2002).
11. M. H. Dietrich *et al.*, Structural and functional features of the reovirus σ1 tail. *J. Virol.* **92**, e00336-18 (2018).
12. K. Reiss *et al.*, The GM2 glycan serves as a functional coreceptor for serotype 1 reovirus. *PLoS Pathog.* **8**, e1003078 (2012).
13. E. S. Barton *et al.*, Junction adhesion molecule is a receptor for reovirus. *Cell* **104**, 441–451 (2001).
14. M. Koehler *et al.*, Glycan-mediated enhancement of reovirus receptor binding. *Nat. Commun.* **10**, 1–14 (2019).
15. E. Kirchner, K. M. Guglielmi, H. M. Strauss, T. S. Dermody, T. Stehle, Structure of reovirus σ1 in complex with its receptor junctional adhesion molecule-A. *PLoS Pathog.* **4**, e1000235 (2008).
16. E. Stettner, M. H. Dietrich, K. Reiss, T. S. Dermody, T. Stehle, Structure of serotype 1 reovirus attachment protein σ1 in complex with junctional adhesion molecule A reveals a conserved serotype-independent binding epitope. *J. Virol.* **89**, 6136–6140 (2015).
17. K. A. Dryden *et al.*, Early steps in reovirus infection are associated with dramatic changes in supramolecular structure and protein conformation: Analysis of virions and subviral particles by cryoelectron microscopy and image reconstruction. *J. Cell Biol.* **122**, 1023–1041 (1993).
18. D. B. Furlong, M. Nibert, B. Fields, Sigma 1 protein of mammalian reoviruses extends from the surfaces of viral particles. *J. Virol.* **62**, 246–256 (1988).
19. D. Alsteens *et al.*, Nanomechanical mapping of first binding steps of a virus to animal cells. *Nat. Nanotechnol.* **12**, 177–183 (2017).
20. C. Bustamante, J. F. Marko, E. D. Siggia, S. Smith, Entropic elasticity of λ-phage DNA. *Science* **265**, 1599–1600 (1994).
21. E. A. Evans, D. A. Calderwood, Forces and bond dynamics in cell adhesion. *Science* **316**, 1148–1153 (2007).
22. E. Evans, K. Ritchie, Dynamic strength of molecular adhesion bonds. *Biophys. J.* **72**, 1541–1555 (1997).
23. C. Rankl *et al.*, Multiple receptors involved in human rhinovirus attachment to live cells. *Proc. Natl. Acad. Sci. U.S.A.* **105**, 17778–17783 (2008).
24. T. Verdorfer *et al.*, Combining in vitro and in silico single-molecule force spectroscopy to characterize and tune cellulosomal scaffoldin mechanics. *J. Am. Chem. Soc.* **139**, 17841–17852 (2017).
25. J. C. Phillips *et al.*, Scalable molecular dynamics on CPU and GPU architectures with NAMD. *J. Chem. Phys.* **153**, 044130 (2020).
26. S. Izrailev, S. Stepaniants, M. Balsera, Y. Oono, K. Schulten, Molecular dynamics study of unbinding of the avidin-biotin complex. *Biophys. J.* **72**, 1568–1581 (1997).
27. O. K. Dudko, G. Hummer, A. Szabo, Intrinsic rates and activation free energies from single-molecule pulling experiments. *Phys. Rev. Lett.* **96**, 108101 (2006).
28. S. Park, K. Schulten, Calculating potentials of mean force from steered molecular dynamics simulations. *J. Chem. Phys.* **120**, 5946–5961 (2004).
29. M. C. Melo, R. C. Bernardi, C. De La Fuente-Nunez, Z. Luthey-Schulten, Generalized correlation-based dynamical network analysis: A new high-performance approach for identifying allosteric communications in molecular dynamics trajectories. *J. Chem. Phys.* **153**, 134104 (2020).
30. M. C. Melo, D. E. Gomes, R. C. Bernardi, Molecular origins of force-dependent protein complex stabilization during bacterial infections. *J. Am. Chem. Soc.* **145**, 70–77 (2022).
31. J. R. Diller *et al.*, Reovirus σ1 conformational flexibility modulates the efficiency of host cell attachment. *J. Virol.* **94**, e01163-20 (2020).
32. M. Eckhardt, B. Gotza, R. Gerardy-Schahn, Mutants of the CMP-sialic acid transporter causing the Lec2 phenotype. *J. Biol. Chem.* **273**, 20189–20195 (1998).
33. N. Arnberg, K. Edlund, A. H. Kidd, G. Wadell, Adenovirus type 37 uses sialic acid as a cellular receptor. *J. Virol.* **74**, 42–48 (2000).
34. P. M. Williams, Analytical descriptions of dynamic force spectroscopy: Behaviour of multiple connections. *Anal. Chim. Acta* **479**, 107–115 (2003).
35. K. Suzuki *et al.*, A conditionally replicative adenovirus with enhanced infectivity shows improved oncolytic potency. *Clin. Cancer Res.* **7**, 120–126 (2001).
36. N. Ruthardt, D. C. Lamb, C. Bräuchle, Single-particle tracking as a quantitative microscopy-based approach to unravel cell entry mechanisms of viruses and pharmaceutical nanoparticles. *Mol. Ther.* **19**, 1199–1211 (2011).
37. A. Berard, K. M. Coombs, Mammalian reoviruses: Propagation, quantification, and storage. *Curr. Protoc. Microbiol.* **14**, 15C. 11.11–15C. 11.18 (2009).
38. G. S. Baer, T. S. Dermody, Mutations in reovirus outer-capsid protein sigma3 selected during persistent infections of L cells confer resistance to protease inhibitor E64. *J. Virol.* **71**, 4921–4928 (1997).
39. B. A. Mainou, T. S. Dermody, Transport to late endosomes is required for efficient reovirus infection. *J. Virol.* **86**, 8346–8358 (2012).
40. R. J. Fecek *et al.*, Production of alexa fluor 488-labeled reovirus and characterization of target cell binding, competence, and immunogenicity of labeled virions. *J. Immunol. Methods* **314**, 30–37 (2006).
41. L. Wildling *et al.*, Linking of sensor molecules with amino groups to amino-functionalized AFM tips. *Bioconjug. Chem.* **22**, 1239–1248 (2011).
42. A. Ebner, P. Hinterdorfer, H. J. Gruber, Comparison of different aminofunctionalization strategies for attachment of single antibodies to AFM cantilevers. *Ultramicroscopy* **107**, 922–927 (2007).
43. V. Dupres *et al.*, Nanoscale mapping and functional analysis of individual adhesins on living bacteria. *Nat. Methods* **2**, 515–520 (2005).
44. H.-J. Butt, M. Jaschke, Calculation of thermal noise in atomic force microscopy. *Nanotechnology* **6**, 1 (1995).
45. C. Bustamante, J. Marko, E. Siggia, S. Smith, Entropic elasticity of lambda-phage DNA. *Proc. Natl. Acad. Sci. U.S.A.* **88**, 10009 (1991).
46. R. Newton *et al.*, Combining confocal and atomic force microscopy to quantify single-virus binding to mammalian cell surfaces. *Nat. Protoc.* **12**, 2275–2292 (2017).
47. C. Rankl *et al.*, "Determination of the kinetic on-and off-rate of single virus–cell interactions" in *Atomic Force Microscopy in Biomedical Research* (Springer, 2011), pp. 197–210.
48. B. Webb, A. Sali, Comparative protein structure modeling using MODELLER. *Curr. Protoc. Bioinformatics* **54**, 5.6.1–5.6.37 (2016).
49. S. Jo, T. Kim, V. G. Iyer, W. Im, CHARMM-GUI: A web-based graphical user interface for CHARMM. *J. Comput. Chem.* **29**, 1859–1865 (2008).
50. W. L. Jorgensen, C. Jenson, Temperature dependence of TIP3P, SPC, and TIP4P water from NPT monte carlo simulations: Seeking temperatures of maximum density. *J. Comput. Chem.* **19**, 1179–1186 (1998).
51. J. V. Ribeiro *et al.*, QwikMD–integrative molecular dynamics toolkit for novices and experts. *Sci. Rep.* **6**, 1–14 (2016).
52. R. B. Best *et al.*, Optimization of the additive CHARMM all-atom protein force field targeting improved sampling of the backbone φ, ψ and side-chain χ1 and χ2 dihedral angles. *J. Chem. Theory Comput.* **8**, 3257–3273 (2012).
53. T. Darden, D. York, L. Pedersen, Particle mesh ewald: An N· log (N) method for ewald sums in large systems. *J. Chem. Phys.* **98**, 10089–10092 (1993).
54. B. W. Silverman, *Density Estimation for Statistics and Data Analysis* (Routledge, 2018).
55. W. Humphrey, A. Dalke, K. Schulten, VMD: Visual molecular dynamics. *J. Mol. Graph.* **14**, 33–38 (1996).
56. M. L. Connolly, Solvent-accessible surfaces of proteins and nucleic acids. *Science* **221**, 709–713 (1983).